Electronic Supplementary Material (ESI) for Journal of Materials Chemistry C.

Supporting Information

Coexistence of Luminescence and Spin-Crossover in 2D Iron(II) Hofmann Clathrates Modulated Through Guest Encapsulation

Rubén Turo-Cortés,[a] Manuel Meneses-Sánchez,[a] Teresa Delgado,[b] Carlos Bartual-Murgui,*[a] M. Carmen Muñoz[c] and J. Antonio Real*[a]

[a]*Departamento de Química Inorgánica, Instituto de Ciencia Molecular (ICMol), Universidad de Valencia, Catedrático José Beltrán 2, 46980 Paterna, Spain*

[b]*PSL University, Chimie Paris Tech, IRCP-CNRS, Paris, 7505, France*

[c]*Departamento de Física Aplicada, Universitat Politècnica de València, Camino de Vera s/n, E-46022, Valencia, Spain.*

EXPERIMENTAL

Materials. All reagents and solvents used, excluding the 4-(anthracene-9-yl)pyridine ligand and Iron(II) p-toluenesulfonate, were obtained from commercial sources and used as received without further purification.

Synthetic procedure. The 4-(anthracene-9-yl)pyridine ligand was synthesized following a procedure previously described.[1]

Single crystals of **AnPyM·XBz** (M = Ag, Au; X = Cl, Br, I, CH_3, NO_2) were grown by slow liquid diffusion in test tubes. The iron salt Fe(p-Tos)$_2$·6H_2O (50.6 mg, 0.1 mmol) and 4-(anthracene-9-yl)pyridine (51.0 mg, 0.2 mmol) were dissolved in 4 mL of MeOH:Xbz (1:3) and added to the bottom of the tube. A spacer of 5 mL of MeOH:Xbz (2:1) was then carefully added. To complete the diffusion, a solution of M(CN)$_2$ (M = Ag (40.0 mg, 0.2 mmol), Au (57.6 mg, 0.2 mmol) in 2 mL of MeOH was added on top. The tube was then sealed and left in darkness for 4 weeks, after that time yellow rhombohedral crystals appear in 70% yield.

AnPyM was obtained by heating the derivative of choice up to the adequate temperature for the guest to leave the network. Check main manuscript and TGA for more information.

Elemental Analysis. Calculated for **AnPyAg** [$C_{42}H_{26}N_6FeAg_2$ (886.3) (%)]: C 56.92; H 2.96; N 9.48. Found (%): C 56.64; H 2.71; N 9.67. Calculated for **AnPyAg·NO_2bz** [$C_{54.2}H_{36.2}N_8O_{4.1}FeAg_2$ (1136.2) (%)]: C 57.27; H 3.21; N 9.89. Found (%): C 57.03; H 3.36; N 9.95. Calculated for **AnPyAg·CH_3bz** [$C_{53.8}H_{41.7}N_6FeAg_2$ (1066.8) (%)] C 60.52; H 3.95; N 7.87. Found (%): C 60.84; H 3.86; N 7.71. Calculated for **AnPyAg·Clbz** [$C_{53.1}H_{35.3}N_6Cl_{1.9}FeAg_2$ (1094.4) (%)]: C 58.27; H 3.25; N 7.68. Found (%): C 58.17; H 3.41; N 7.75. Calculated for **AnPyAg·Brbz** [$C_{53.3}H_{35.4}N_6Br_{1.9}FeAg_2$ (1181.4) (%)]: C 54.16; H 3.03; N 7.11. Found (%): C 53.96; H 2.97; N 7.27. Calculated for **AnPyAg·Ibz** [$C_{51.6}H_{34}N_6I_{1.6}FeAg_2$ (1211.7) (%)]: C 51.10; H 2.83; N 2.83. Found (%): C 51.34; H 2.74; N 6.84. Calculated for **AnPyAu** [$C_{42}H_{26}N_6FeAu_2$ (1064.5) (%)]: C 47.39; H 1.46; N 7.89. Found (%): C 47.07; H 1.63; N 7.93. Calculated for **AnPyAu·NO_2bz** [$C_{53.8}H_{35.8}N_8FeAu_2$ (1305.7) (%)]: C 49.45; H 2.77; N 8.53. Found (%): C 49.19; H 2.96; N 8.91. Calculated for **AnPyAu·CH_3bz** [$C_{53.8}H_{41.7}N_6FeAu_2$ (1245.0) (%)]: C 51.86; H 3.38; N 6.75. Found (%): C 51.39; H 3.74; N 6.97. Calculated for **AnPyAu·Clbz** [$C_{51.6}H_{34}N_6Cl_{1.6}FeAu_2$ (1244.5) (%)]: C 49.80; H 2.76; N 6.75. Found (%): C 50.06; H 2.79; N 6.62. Calculated for **AnPyAu·Clbz** [$C_{51}H_{33.5}N_6Br_{1.5}FeAu_2$ (1300.0) (%)]: C 47.12; H 2.60; N 6.46. Found (%): C 46.97; H 2.71; N 6.23. Calculated for **AnPyAu·Ibz** [$C_{50.5}H_{33.1}N_6I_{1.4}FeAu_2$ (1354.15) (%)]: C 44.81; H 2.47; N 6.20. Found (%): C 44.27; H 2.03; N 6.64.

Physical characterization

Elemental analyses (C, H and N) were performed with a CE Instruments EA 1110 CHNS Elemental analyzer.

Magnetic measurements were performed with a Quantum Design MPMS-XL-5 SQUID magnetometer working in the 2 to 400 K temperature range at 1 K/min with an applied magnetic field of 1 T. Experimental susceptibilities were corrected for diamagnetism of the constituent atoms using Pascal's constants. LIESST measurements were performed by cooling the sample to 10 K and irradiating with laser at 633 nm (red) or 532 nm (green). Upon saturation of the sample the laser was switched off and the temperature was increased at 0.3 K/min.

Calorimetric measurements were performed using a differential scanning calorimeter Mettler Toledo DSC 821e. Low temperatures were obtained with an aluminium block attached to the sample holder, refrigerated with a flow of liquid nitrogen and stabilized at a temperature of 110 K. The sample holder was kept in a dry box under a flow of dry nitrogen gas to avoid water condensation. The measurements were carried out at 10 K/min using around 15 mg of crystalline samples sealed in aluminium pans with a mechanical crimp. Temperature and heat flow calibrations were made with standard samples of indium by using its melting transition (429.6K, 28.45 J/g). An overall accuracy of ±0.2 K in temperature and ±2% in the heat capacity is estimated. The uncertainty increases for the determination of the anomalous enthalpy and entropy due to the subtraction of an unknown baseline.

Powder X-ray diffraction measurements were performed on a PANalytical Empyrean X-ray powder diffractometer (monochromatic CuKα radiation) in capillary measurement mode.

Single crystal X-ray measurements. Single crystals were mounted on a glass fiber using a viscous hydrocarbon oil to coat the crystal and then transferred directly to the cold nitrogen stream for data collection. X-ray data were collected on a Supernova diffractometer equipped with a graphite-monochromated Enhance (Mo) X-ray Source (λ = 0.71073 Å). The program CrysAlisPro, Oxford Diffraction Ltd., was used for unit cell determinations and data reduction. Empirical absorption correction was performed using spherical harmonics, implemented in the SCALE3 ABSPACK scaling algorithm. The structures were solved by direct methods using SHELXS-2014 and refined by full matrix least-squares on F 2 using SHELXL-2014.[2] Non-hydrogen atoms were refined anisotropically, and hydrogen atoms were placed in calculated positions refined using idealized geometries (riding model) and assigned fixed isotropic displacement parameters. CCDC 2166356-2166379 contain the supplementary crystallographic data for this article. These data can be obtained free of charge from The Cambridge Crystallographic Data Centre via www.ccdc.cam.ac.uk/ data_request/cif.

TGA experiments were carried out with a TA instruments TGA550 device equipped with a Pt/Rh oven (Tmax = 1000°C). A flow of dry nitrogen gas was used as the atmosphere during the measurement. The samples were measured in a Pt pan.

*Absorption spectroscopy***.** The single crystals are mounted in a copper plate with a previously made hole of the same size. To attach them, silver-nanoparticles paste (Agar scientific) is used to ensure the thermal conductivity. The spectra are recorded with the double beam UV/Vis/NIR spectrophotometer Varian Cary 6000. The temperature is tuned with a closed cycle cryostat with a cooling-heating rate of 10 K/min.

Quantum yield. A Quantum Efficiency Measurement System (EQE/IQE) (Newport QUANTX-300) was used to estimate the quantum yield of all the samples. As an excitation source a 365 nm LED (Thorlabs) was used.

Fluorescence. The room temperature fluorescence spectra of all samples were recorded in a fluorescence spectrophotometer Varian Cary Eclipse.

Variable temperature emission spectra. Fluorescence measurements at variable temperature were carried out using a closed-cycle He-flow cryostat (Sumitomo Cryogenics HC-4E) attached with a Lakeshore 340 temperature controller. The samples were cooled from room temperature to to 15 K. The heating-cooling rate was set at 10 K/min. The excitation in most of the temperature cycles is a 365 nm LED (Thorlabs). A detection filter was used to cut the excitation source. The emission was detected with a CCD camera (Roper Pixis 100) coupled to a visible monochromator (Acton Spectra Pro, Princeton Instruments, 300 grooves per mm, centred at 600 nm). The emission intensity was integrated as a function of temperature.

References:

1 W. J. Ramsay, F. T. Szczypin, H. Weissman, T. K. Ronson, M. M. J Smulders, B. oris Rybtchinski, J. R. Nitschke, W. J. Ramsay, F. Szczypin, D. KRonson, J. R. Nitschke, D. eissman and B. Rybtchinski, *Angew. Chemie Int. Ed.*, 2015, **54**, 5636–5640.

2 G. M. Sheldrick, *Acta Crystallogr. Sect. A Found. Adv.*, 2015, **71**, 3–8.

Figure S1. Thermogravimetric analysis for all the **AnPyM·XBz** derivatives.

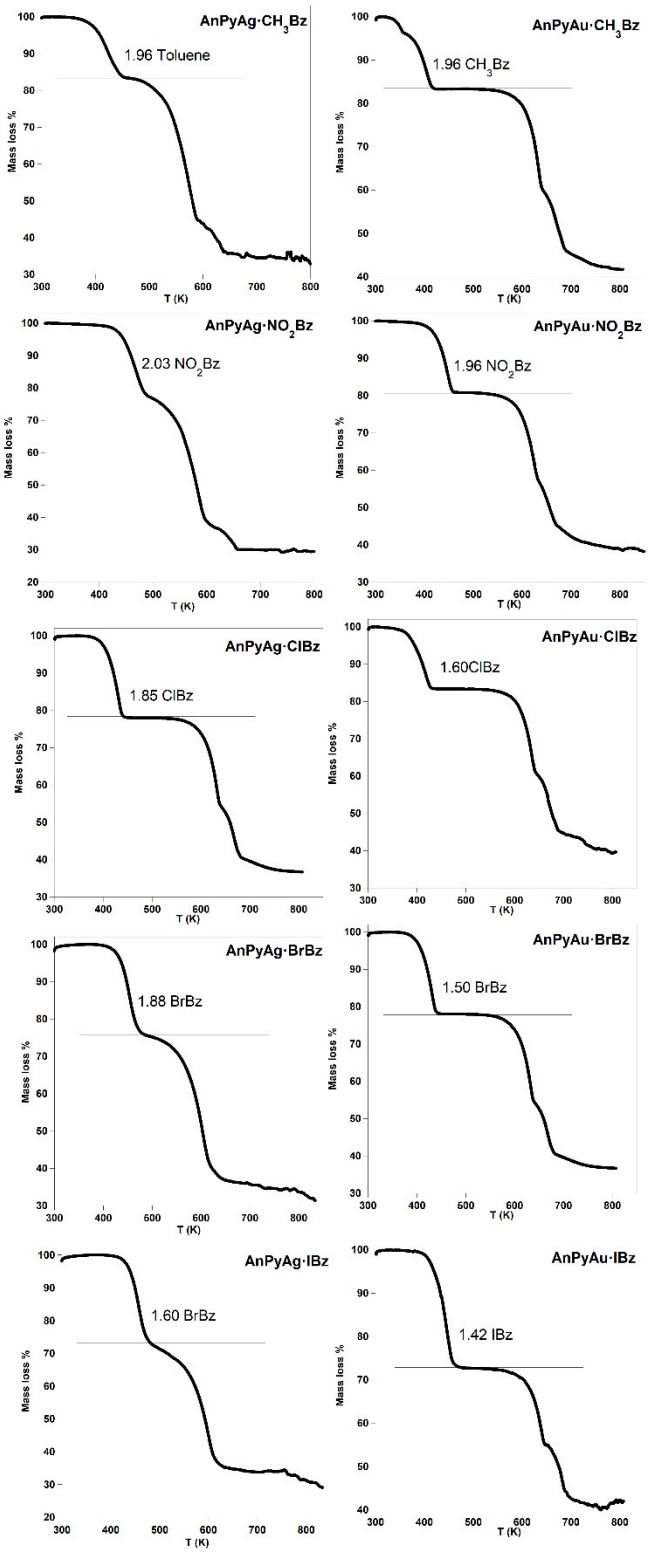

Figure S2. XRPD patterns of a) **AnPyAu·CH_3Bz** and b) **AnPyAu·ClBz** measured in the mother liquor (green curves) and several hours after exposing to air (red lines) which shows the transformation from the triclinic to the orthorhombic structures. The patterns simulated from the triclinic (top) and orthorhombic (bottom) structures are depicted (black curves) for comparison. In the case of the

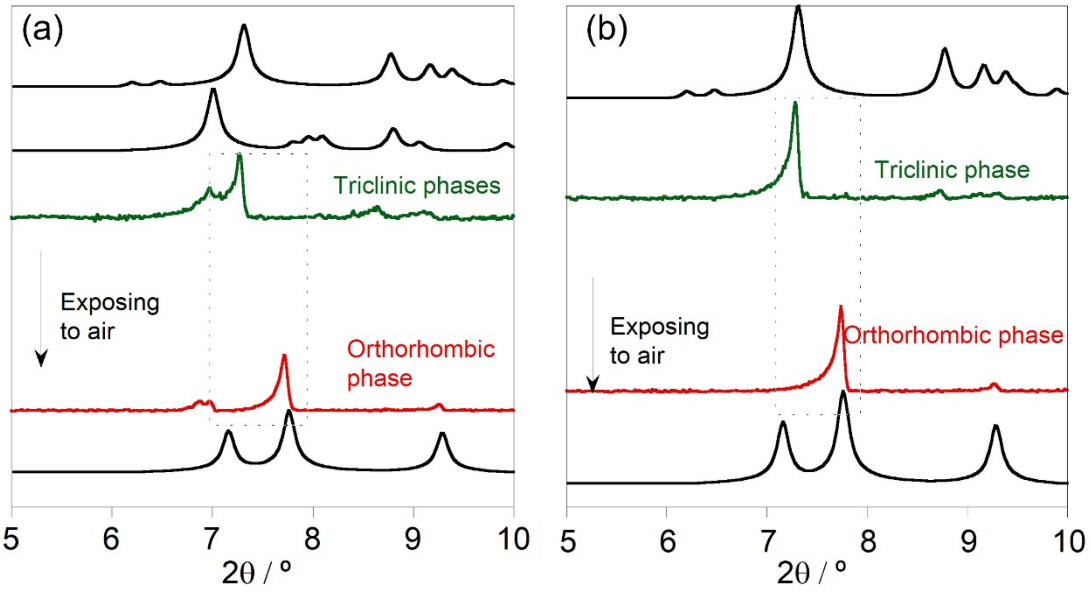

orthorhombic simulated pattern, that obtained from **AnPyAu·BrBz** was used as reference.

Figure S3. XRPD patterns for the M = Ag (left) and the M = Au (right) derivatives of the **AnPyM·XBz** family**.** The unsolvated counterparts (green curves), **NiAnPyAu·NO_2Bz** and typical simulated orthorhombic patterns of **AnPyM·XBz** (black curves) are also displayed for comparison (the change in intensity ratio of peaks between 6-10° may be explained by preferential orientations of the measured crystals).

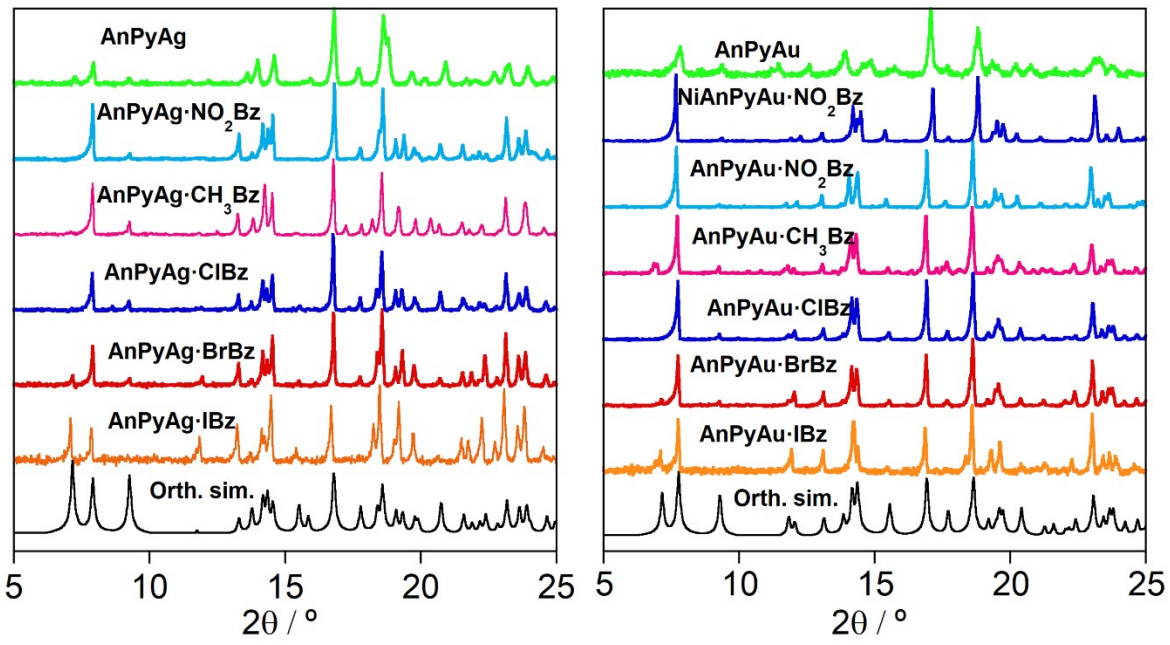

Figure S4. Thermal magnetic behavior of a) **AnPyAu·CH_3Bz** and b) **AnPyAu·ClBz** measured in the mother liquor (green curves) and several hours after exposing to air (red lines).

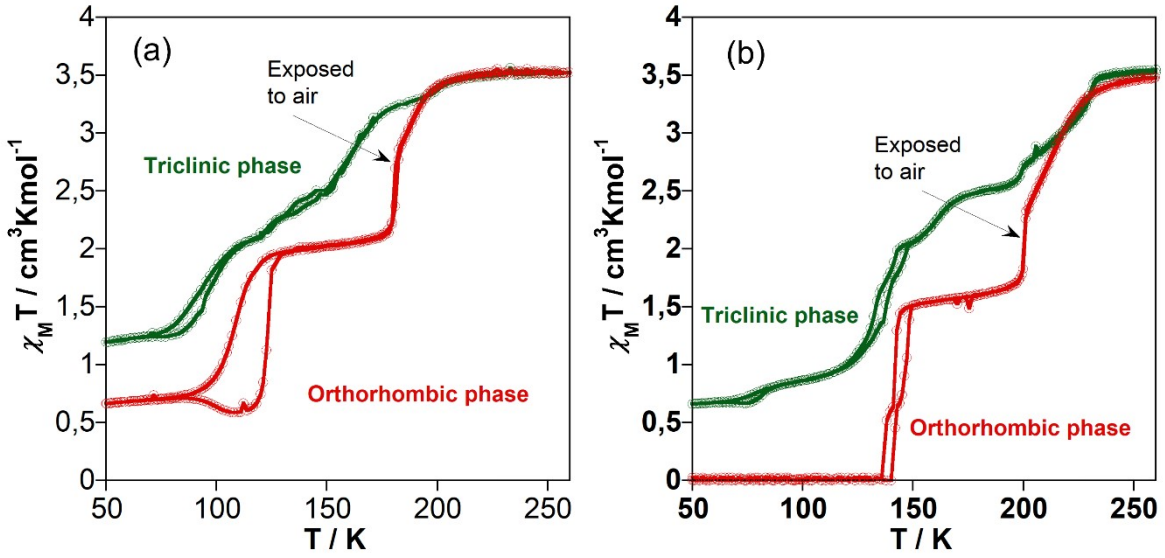

Figure S5. Thermal dependence magnetic behavior of the **AnPyAg** and **AnPyAu** unsolvated

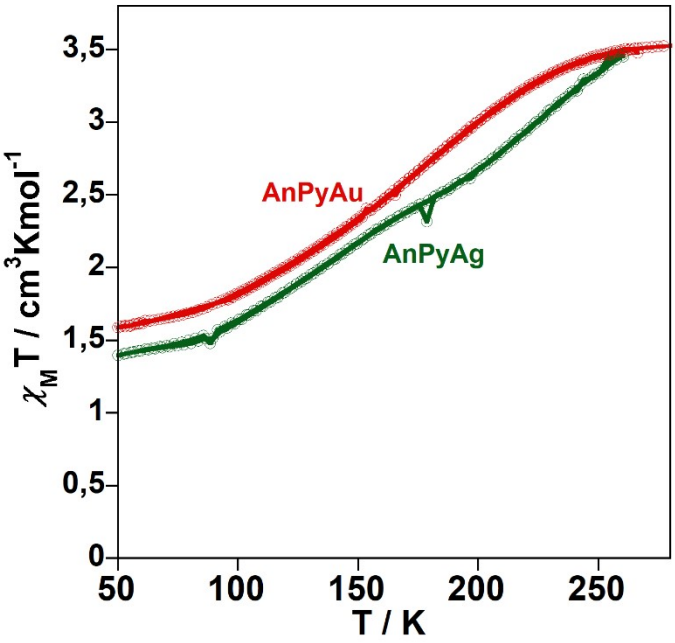

counterparts.

Figure S6. DSC curves for compounds **AnPyAg·XBz** (X=Cl, Br; CH_3, NO_2) and **AnPyAu·NO2Bz** measured at 10 K/min. The blue and red lines represent the cooling and heating modes, respectively. Magnetic curves are also represented for comparison.

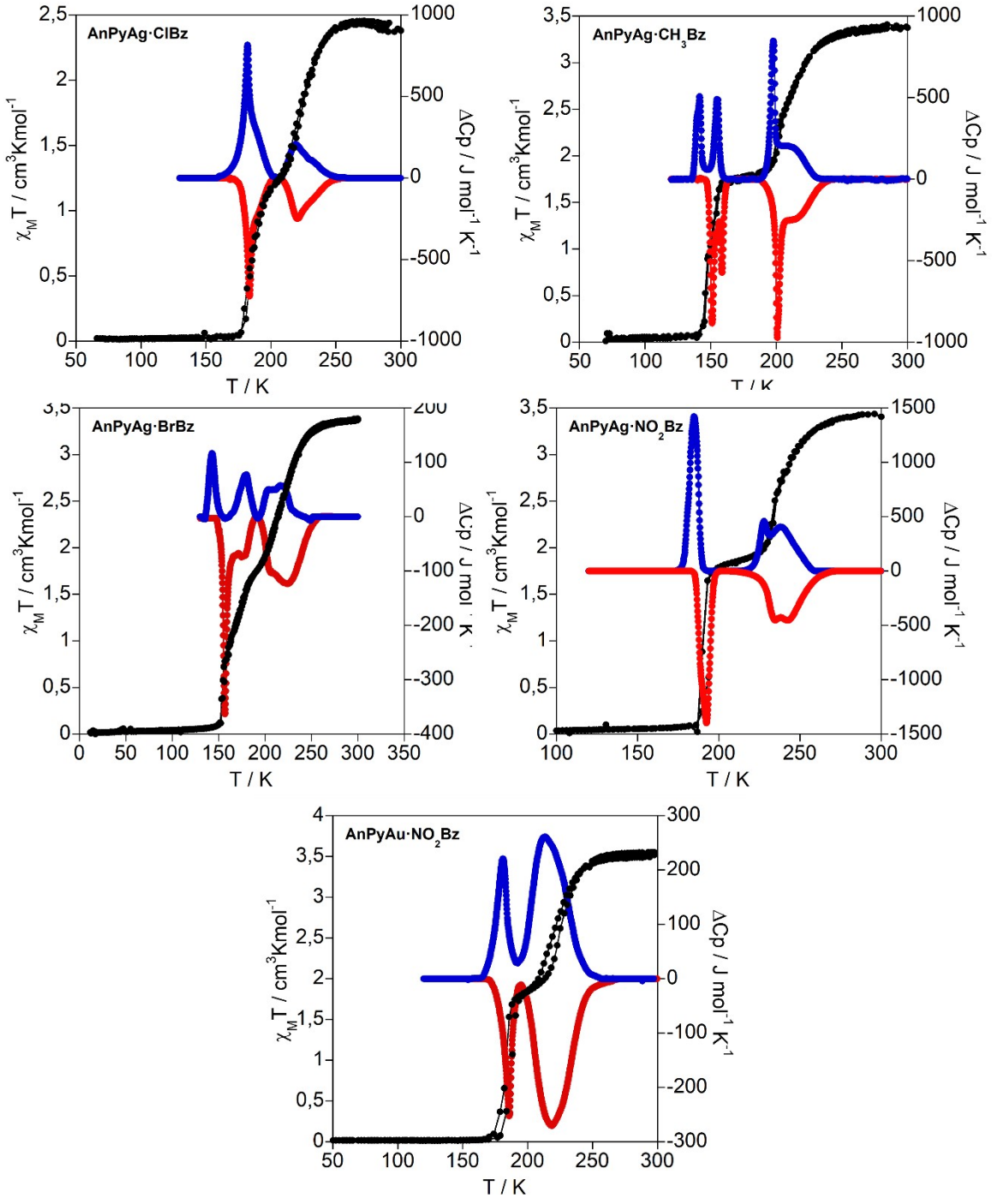

Table S1. Thermodinamic parameters extracted from the calorimetric measurements.

Figure S7. Thermal dependent magnetic (red (cooling 1 K/min) and black (heating after photoexcitation 0.3 K/min) curves) and photomagnetic properties (green curves (λ_{irrad} = 532 nm)) of the **AnPyM·XBz** derivatives.

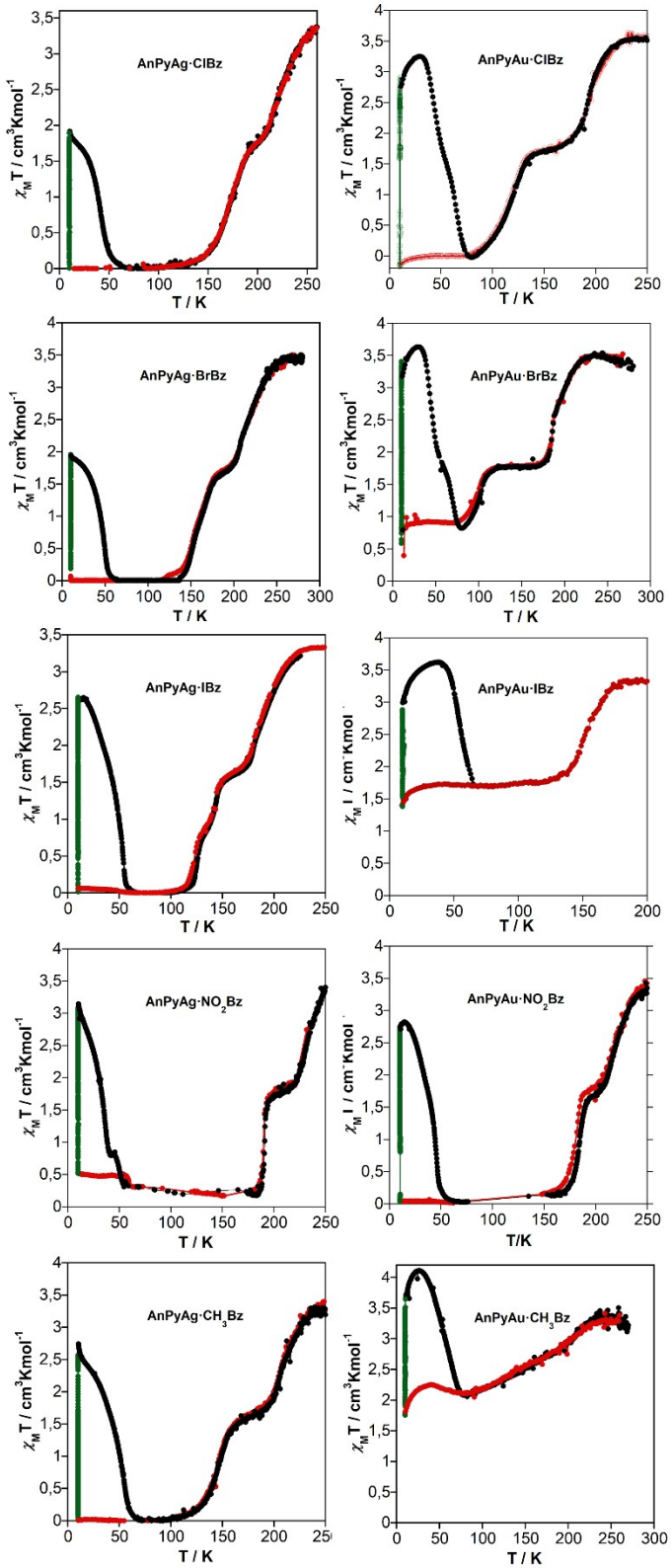

Table S2. Crystal data for **AnPyAg·NO_2Bz**.

	$AgNO_2$Bz_120 K	**$AgNO_2$Bz_210 K**	**$AgNO_2$Bz_290 K**
Empirical formula	$C_{52.8}H_{35}N_{7.8}O_{3.6}Ag_2Fe$		
*M*r	1107.87		
Crystal system	orthorhombic		
Space group	*Cccm*		
a (Å)	14.0939(4)	14.3894(11)	14.7826(5)
b (Å)	22.2731(7)	22.2526(14)	22.3755(6)
c (Å)	14.7007(4)	14.9826(7)	15.0486(4)
V (Å^3)	4614.8(2)	4797.5(5)	4977.6(3)
Z	4		
D_c (mg cm^{-3})	1.595	1.534	1.478
F(000)	2221		
μ (Mo-K_α) (mm^{-1})	1.206	1.160	1.118
Crystal size (mm)	0.05x0.10x0.20		
No. of total reflections	2518	3197	3480
No. of reflections [$I>2\sigma(I)$]	1888	1343	1758
R [$I>2\sigma(I)$]	0.0553	0.0804	0.0690
wR [$I>2\sigma(I)$]	0.1522	0.1997	0.1875
S	1.061	0.965	0.993

$R_1 = \Sigma \, ||Fo| - |Fc|| \, / \, \Sigma \, |Fo|$; $wR = [\, \Sigma \, [w(Fo^2 - Fc^2)^2] \, / \, \Sigma \, [w(Fo^2)^2]]^{1/2}$.
$w = 1/ \, [\sigma^2(Fo^2) + (m \, P)^2 + n \, P]$ where $P = (Fo^2 + 2Fc^2) \, / \, 3$;
m = 0.0807 (**1**), 0.1032 (**2**) and 0.1153 (**3**);
n = 25.3803 (**1**), 0.0000 (**2**) and 0.0000 (**3**)

Table S3. Selected bond lengths [Å] and angles [°] for **AnPyAg·NO_2Bz**.

	$AgNO_2$Bz_120 K	**$AgNO_2$Bz_210 K**	**$AgNO_2$Bz_290 K**
Fe-N(1)	1.932(4)	2.038(6)	2.139(5)
Fe-N(2)	2.000(6)	2.099(10)	2.228(6)
Ag-C(1)	2.053(5)	2.063(8)	2.058(6)
N(1)-Fe-N(2)	90.8(2)	88.9(3)	88.6(2)
C(1)-Ag-C(1)	171.2(3)	170.3(5)	170.6(3)

Table S4. Crystal data for **AnPyAg·CH$_3$Bz**.

	AgCH$_3$Bz_120 K	**AgCH$_3$Bz_170 K**	**AgCH$_3$Bz_260 K**
Empirical formula	$C_{54.6}H_{40.4}N_6Ag_2Fe$		
*M*r	1052.12		
Crystal system	orthorhombic		
Space group	*Pccn*		
a (Å)	14.3993(3)	14.6888(7)	22.3526(10)
b (Å)	22.2116(4)	22.2043(7)	14.9673(6)
c (Å)	14.5770(4)	14.7091(5)	14.9037(6)
V (Å^3)	4662.2(2)	4797.4(3)	4986.2(4)
Z	4		
D_c (mg cm^{-3})	1.499	1.457	1.402
F(000)	2120		
μ (Mo-K$_\alpha$) (mm^{-1})	1.182	1.149	1.106
Crystal size (mm)	0.05x0.20x0.20		
No. of total reflections	6030	6381	6619
No. of reflections [$I>2\sigma(I)$]	3920	4037	2811
R [$I>2\sigma(I)$]	0.0550	0.0971	0.0565
wR [$I>2\sigma(I)$]	0.1140	0.1803	0.1089
S	1.037	1.100	0.920

$R_1 = \Sigma \, ||Fo| - |Fc|| \, / \, \Sigma \, |Fo|$; $wR = [\, \Sigma \, [w(Fo^2 - Fc^2)^2] \, / \, \Sigma \, [w(Fo^2)^2]]^{1/2}$.
$w = 1/ \, [\sigma^2(Fo^2) + (m \, P)^2 + n \, P]$ where $P = (Fo^2 + 2Fc^2) \, / \, 3$;
m = 0.0454 (**1**), 0.0000 (**2**) and 0.0385 (**3**);
n = 5.6480 (**1**), 71.7043 (**2**) and 0.0000 (**3**)

Table S5. Selected bond lengths [Å] and angles [°] for **AnPyAg·CH$_3$Bz**

	AgCH$_3$Bz_120 K	**AgCH$_3$Bz_170 K**	**AgCH$_3$Bz_260 K**
Fe-N(1)	1.950(4)	2.032(7)	2.140(4)
Fe-N(2)	1.944(4)	2.044(7)	2.144(4)
Fe-N(3)	2.006(4)	2.119(6)	2.212(4)
Ag-C(1)	2.073(5)	2.058(9)	2.058(5)
Ag-C(2)	2.062(5)	2.096(9)	2.058(5)
N(1)-Fe-N(2)	89.4(2)	88.3(3)	88.4(2)
N(1)-Fe-N(3)	89.46(14)	88.6(2)	88.55(14)
N(2)-Fe-N(3)	90.47(14)	90.5(2)	90.24(14)
C(1)-Ag-C(2)	170.4(2)	169.2(3)	170.3(2)

Table S6. Crystal data for **AnPyAg·ClBz**

	AgClBz_120 K	**AgClBz_207 K**	**AgClBz_280 K**
Empirical formula	$C_{51.6}H_{34}Cl_{1.6}N_6Ag_2Fe$		
*M*r	1066.36		
Crystal system	orthorhombic		
Space group	*Ccc*2	*Pmna*	*Ccc*2
a (Å)	14.1974(3)	14.9087(3)	14.707(7)
b (Å)	22.2274(6)	14.4938(3)	22.230(11)
c (Å)	14.7169(4)	22.2153(5)	15.113(7)
V (Å^3)	4644.2(2)	4800.4(2)	4941(4)
Z	4		
D_c (mg cm^{-3})	1.525	1.475	1.434
F(000)	2131		
μ (Mo-K$_\alpha$) (mm^{-1})	1.277	1.235	1.200
Crystal size (mm)	0.04x0.30x0.30		
No. of total reflections	8301	5153	5051
No. of reflections [$I>2\sigma(I)$]	8029	3143	3228
R [$I>2\sigma(I)$]	0.0267	0.0673	0.0969
wR [$I>2\sigma(I)$]	0.0685	0.1978	0.2337
S	1.065	1.067	1.024

$R_1 = \Sigma \, ||Fo| - |Fc|| \, / \, \Sigma \, |Fo|$; $wR = [\, \Sigma \, [w(Fo^2 - Fc^2)^2] \, / \, \Sigma \, [w(Fo^2)^2]]^{1/2}$.
$w = 1/ \, [\sigma^2(Fo^2) + (m \, P)^2 + n \, P]$ where $P = (Fo^2 + 2Fc^2) \, / \, 3$;
m = 0.0321 (**1**), 0.1001 (**2**) and 0.1113 (**3**);
n = 6.1118 (**1**), 8.0766 (**2**) and 137.4962 (**3**)

Table S7. Selected bond lengths [Å] and angles [°] for **AnPyAg·ClBz**.

	AgClBz_120 K	**AgClBz_207 K**	**AgClBz_280 K**
Fe-N(1)	1.933(2)		2.16(2)
Fe-N(2)	1.936(2)		2.09(2)
Fe-N(3)	2.006(2)		2.235(7)
Fe(1)-N(1)		1.987(4)	
Fe(1)-N(3)		2.075(6)	
Fe(2)-N(2)		2.113(4)	
Fe(2)-N(4)		2.181(6)	
Ag-C(1)	2.040(3)	2.065(5)	2.01(2)
Ag-C(2)	2.049(3)	2.046(6)	2.07(3)
N(1)-Fe-N(2)	89.83(7)		89.6(7)
N(1)-Fe-N(3)	90.28(10)		91.5(7)
N(2)-Fe-N(3)	89.17(10)		91.3(7)
N(1)-Fe(1)-N(3)		89.0(2)	
N(2)-Fe(2)-N(4)		91.6(2)	
C(1)-Ag-C(2)	171.34(9)	171.4(2)	169.8(8)

Table S8. Crystal data for **AnPyAg·BrBz**.

	AgBrBz_120 K	**AgBrBz_192 K**	**AgBrBz_280 K**
Empirical formula	$C_{52.8}H_{35}Br_{1.8}N_6Ag_2Fe$		
*M*r	1168.89		
Crystal system	orthorhombic		
Space group	*Ccc*2	*Pmna*	*Ccc*2
a (Å)	14.3261(7)	14.8634(6)	14.7990(7)
b (Å)	22.2063(9)	14.5587(8)	22.3435(10)
c (Å)	14.6300(7)	14.5587(8)	15.0463(5)
V (Å^3)	4654.2(4)	4813.8(4)	4975.2(4)
Z	4		
D_c (mg cm^{-3})	1.668	1.613	1.561
F(000)	2307		
μ (Mo-K$_\alpha$) (mm^{-1})	2.729	2.639	2.553
Crystal size (mm)	0.05x0.20x0.40		
No. of total reflections	3919	5168	3943
No. of reflections [$I>2\sigma(I)$]	3488	3089	2860
R [$I>2\sigma(I)$]	0.0368	0.0751	0.0412
wR [$I>2\sigma(I)$]	0.0909	0.2134	0.0607
S	1.062	1.064	0.930

$R_1 = \Sigma \, ||Fo| - |Fc|| \, / \, \Sigma \, |Fo|$; $wR = [\, \Sigma \, [w(Fo^2 - Fc^2)^2] \, / \, \Sigma \, [w(Fo^2)^2]]^{1/2}$.
$w = 1/ \, [\sigma^2(Fo^2) + (m \, P)^2 + n \, P]$ where $P = (Fo^2 + 2Fc^2) \, / \, 3$;
m = 0.0478 (**1**), 0.1098 (**2**) and 0.0090 (**3**);
n = 0.0000 (**1**), 5.1486 (**2**) and 0.0000 (**3**)

Table S9. Selected bond lengths [Å] and angles [°] for **AnPyAg·BrBz**.

	AgBrBz_120 K	**AgBrBz_192 K**	**AgBrBz_280 K**
Fe-N(1)	1.995(6)		2.146(7)
Fe-N(2)	1.894(6)		2.102(8)
Fe-N(3)	2.012(4)		2.229(4)
Fe(1)-N(1)		2.137(5)	
Fe(1)-N(3)		2.200(6)	
Fe(2)-N(2)		1.964(5)	
Fe(2)-N(4)		2.042(6)	
Ag-C(1)	2.015(7)	2.067(6)	2.048(9)
Ag-C(2)	2.106(8)	2.075(6)	2.119(10)
N(1)-Fe-N(2)	89.3(2)		88.0(2)
N(1)-Fe-N(3)	87.2(2)		87.7(3)
N(2)-Fe-N(3)	92.7(2)		93.8(3)
N(1)-Fe(1)-N(3)		91.1(2)	
N(2)-Fe(2)-N(4)		90.3(2)	
C(1)-Ag-C(2)	171.3(2)	170.9(3)	170.9(2)

Table S10. Crystal data for **AnPyAu·NO$_2$Bz**.

	AuNO$_2$Bz_150 K	**AuNO$_2$Bz_200 K**	**AuNO$_2$Bz_280 K**
Empirical formula	$C_{50.4}H_{33}N_{7.4}O_{2.8}Au_2Fe$		
*M*r	1236.82		
Crystal system	orthorhombic		
Space group	*Cccm*		
a (Å)	14.0279(3)	14.2233(4)	14.5414(5)
b (Å)	22.9617(8)	22.9389(6)	22.9006(8)
c (Å)	14.4747(3)	14.8302(3)	15.0008(6)
V (Å^3)	4662.4(2)	4838.6(2)	4995.3(3)
Z	4		
D_c (mg cm^{-3})	1.762	1.698	1.645
F(000)	2374		
μ (Mo-K$_\alpha$) (mm^{-1})	6.634	6.392	6.192
Crystal size (mm)	0.10x0.20x0.40		
No. of total reflections	2446	2540	2638
No. of reflections [$I>2\sigma(I)$]	2048	1988	1986
R [$I>2\sigma(I)$]	0.0394	0.0407	0.0454
wR [$I>2\sigma(I)$]	0.1027	0.1116	0.1241
S	1.077	1.067	1.059

$R_1 = \Sigma \, ||Fo| - |Fc|| \, / \, \Sigma \, |Fo|$; $wR = [\, \Sigma \, [w(Fo^2 - Fc^2)^2] \, / \, \Sigma \, [w(Fo^2)^2]]^{1/2}$.
$w = 1/ \, [\sigma^2(Fo^2) + (m \, P)^2 + n \, P]$ where $P = (Fo^2 + 2Fc^2) \, / \, 3$;
m = 0.0458 (**1**), 0.0558 (**2**) and 0.0635 (**3**);
n = 76.5826 (**1**), 29.0573 (**2**) and 19.6285 (**3**)

Table S11. Selected bond lengths [Å] and angles [°] for **AnPyAu·NO$_2$Bz**.

	AuNO$_2$Bz_150 K	**AuNO$_2$Bz_200 K**	**AuNO$_2$Bz_280 K**
Fe-N(1)	1.917(5)	2.027(5)	2.144(5)
Fe-N(2)	2.008(7)	2.126(7)	2.224(7)
Au-C(1)	1.990(7)	1.994(7)	1.981(7)
N(1)-Fe-N(2)	90.1(2)	90.6(2)	90.6(2)
C(1)-Au-C(1)	176.4(3)	175.8(3)	176.1(4)

Table S12. Crystal data for **AnPyAu·CH_3Bz**.

	$AuCH_3Bz$_95 K	**$AuCH_3Bz$_140 K**	**$AuCH_3Bz$_260 K**
Empirical formula	$C_{60.67}H_{47.33}N_6Au_2Fe$		
*M*r	1310.16		
Crystal system	triclinic		
Space group	*P*-1		
a (Å)	13.2270(3)	13.2644(4)	13.3503(8)
b (Å)	13.7058(4)	13.7480(6)	13.8787(9)
c (Å)	23.1363(8)	23.2743(8)	23.5204(12)
α (°)	74.044(3)	74.165(3)	74.237(5)
β (°)	83.768(2)	83.500(3)	83.785(4)
γ (°)	70.263(2)	70.209(3)	70.718(6)
V (Å^3)	3795.2(2)	3841.0(3)	3958.0(4)
Z	3		
D_c (mg cm^{-3})	1.720	1.699	1.649
F(000)	1912		
μ (Mo-K_α) (mm^{-1})	6.113	6.040	5.862
Crystal size (mm)	0.10x0.20x0.20		
No. of total reflections	15063	15191	15371
No. of reflections [$I>2\sigma(I)$]	11469	11516	11633
R [$I>2\sigma(I)$]	0.0428	0.0474	0.0393
wR [$I>2\sigma(I)$]	0.0594	0.0658	0.0714
S	1.048	1.060	1.034

$R_1 = \Sigma \, ||Fo| - |Fc|| \, / \, \Sigma \, |Fo|$; $wR = [\, \Sigma \, [w(Fo^2 - Fc^2)^2] \, / \, \Sigma \, [w(Fo^2)^2]]^{1/2}$.
$w = 1/ \, [\sigma^2(Fo^2) + (m \, P)^2 + n \, P]$ where $P = (Fo^2 + 2Fc^2) \, / \, 3$;
m = 0.0110 (**1**), 0.0045 (**2**) and 0.0237 (**3**);
n = 0.7800 (**1**), 4.3468 (**2**) and 2.2548 (**3**)

Table S13. Selected bond lengths [Å] and angles [°] for **AnPyAu·CH_3Bz**.

	$AuCH_3Bz$_95 K	**$AuCH_3Bz$_140 K**	**$AuCH_3Bz$_260 K**
Fe(1)-N(1)	2.016(5)	2.040(5)	2.151(4)
Fe(1)-N(2)	2.015(5)	2.036(6)	2.139(4)
Fe(1)-N(3)	2.035(6)	2.049(8)	2.172(4)
Fe(1)-N(4)	2.015(5)	2.031(6)	2.144(5)
Fe(1)-N(7)	2.108(4)	2.126(5)	2.222(4)
Fe(1)-N(8)	2.105(4)	2.124(5)	2.229(4) .
Fe(2)-N(5)	2.079(5)	2.151(5)	2.154(5)
Fe(2)-N(6)	2.056(5)	2.122(5)	2.135(4)
Fe(2)-N(9)	2.141(5)	2.213(5)	2.228(4)
Au(1)-C(3)	2.032(8)	2.041(10)	1.992(6)
Au(2)-C(2)	1.981(6)	1.980(7)	2.001(6)
Au(3)-C(4)	1.994(7)	1.981(7)	1.985(6)
Au(3)-C(5)	1.979(6)	1.982(7)	1.975(6)
Au(4)-C(1)	1.983(7)	1.990(7)	1.983(6)
Au(4)-C(6)	1.991(7)	2.004(7)	1.994(6)
N(1)-Fe(1)-N(2)	90.6(2)	90.9(2)	90.5(2)
N(1)-Fe(1)-N(3)	176.2(2)	175.6(2)	175.9(2)
N(1)-Fe(1)-N(4)	89.7(2)	89.2(2)	90.1(2)
N(1)-Fe(1)-N(7)	88.3(2)	88.0(2)	87.9(2)
N(1)-Fe(1)-N(8)	86.3(2)	85.9(2)	85.9(2)
N(2)-Fe(1)-N(3)	89.1(2)	89.2(2)	89.8(2)
N(2)-Fe(1)-N(4)	179.6(2)	179.4(2)	178.8(2)
N(2)-Fe(1)-N(7)	91.2(2)	91.0(2)	90.9(2)
N(2)-Fe(1)-N(8)	91.8(2)	92.1(2)	92.2(2)
N(3)-Fe(1)-N(4)	90.6(2)	90.7(2)	89.8(2)
N(3)-Fe(1)-N(7)	95.5(2)	96.4(2)	96.2(2)
N(3)-Fe(1)-N(8)	89.9(2)	89.7(2)	90.0(2)
N(4)-Fe(1)-N(7)	88.5(2)	88.4(2)	88.1(2)
N(4)-Fe(1)-N(8)	88.6(2)	88.5(2)	88.9(2)
N(7)-Fe(1)-N(8)	173.8(2)	173.2(2)	173.1(2)
N(5)-Fe(2)-N(6)	89.5(2)	89.2(2)	88.5(2)
N(5)-Fe(2)-N(9)	88.9(2)	89.5(2)	89.4(2)
N(6)-Fe(2)-N(9)	87.3(2)	87.0(2)	87.5(2)
C(3)-Au(1)-C(3)	180.0	180.0	180.0
C(2)-Au(2)-C(2)	180.0	180.0	180.0
C(4)-Au(3)-C(5)	173.9(2)	174.5(3)	174.5(2)
C(1)-Au(4)-C(6)	177.9(2)	178.4(3)	177.6(2)

Table S14. Crystal data for **AnPyAu·ClBz**.

	AuClBz_110 K	**AuClBz_180 K**	**AuClBz_260 K**
Empirical formula	$C_{54}H_{36}N_6Cl_2Au_2Fe$		
*M*r	1289.57		
Crystal system	triclinic		
Space group	*P*-1		
a (Å)	15.3053(6)	15.6161(5)	13.4930(5)
b (Å)	18.2506(6)	18.2748(4)	13.6762(4)
c (Å)	19.4681(7)	19.6811(5)	15.6627(5)
α (°)	90.757(3)	90.508(2)	86.165(2)
β (°)	106.614(3)	106.812(2)	65.442(3)
γ (°)	108.244(3)	108.781(2)	86.215(2)
V (Å^3)	4917.4(3)	5057.9(2)	2620.6(2)
Z	4		2
D_c (mg cm^{-3})	1.742	1.693	1.634
F(000)	2480		1240
μ (Mo-K$_\alpha$) (mm^{-1})	6.394	6.217	5.999
Crystal size (mm)	0.10x0.20x0.30		
No. of total reflections	18975	20602	10916
No. of reflections [$I>2\sigma(I)$]	12498	14434	7873
R [$I>2\sigma(I)$]	0.0603	0.0497	0.0461
wR [$I>2\sigma(I)$]	0.1317	0.1097	0.1051
S	1.046	1.059	1.051

$R_1 = \Sigma \, ||Fo| - |Fc|| \, / \, \Sigma \, |Fo|$; $wR = [\, \Sigma \, [w(Fo^2 - Fc^2)^2] \, / \, \Sigma \, [w(Fo^2)^2]]^{1/2}$.
$w = 1/ \, [\sigma^2(Fo^2) + (m \, P)^2 + n \, P]$ where $P = (Fo^2 + 2Fc^2) \, / \, 3$;
m = 0.0486 (**1**), 0.0455 (**2**) and 0.0468 (**3**);
n = 29.0248 (**1**), 16.8124 (**2**) and 8.5045 (**3**)

Table S15. Selected bond lengths [Å] and angles [°] for **AnPyAu·ClBz**.

	AuClBz_110 K	**AuClBz_180 K**	**AuClBz_260 K**
Fe(1)-N(1)	1.962(8)	1.938(6)	
Fe(1)-N(2)	1.953(9)	1.942(6)	
Fe(1)-N(9)	2.003(9)	2.011(6)	
Fe(2)-N(3)	1.955(9)	2.162(7)	
Fe(2)-N(4)	1.958(9)	2.156(6)	
Fe(2)-N(5)	1.951(10)	2.147(6)	
Fe(2)-N(6)	1.963(9)	2.161(6)	
Fe(2)-N(10)	2.027(9)	2.203(6)	
Fe(2)-N(11)	2.021(9)	2.203(6)	
Fe(3)-N(7)	2.153(9)	2.134(6)	
Fe(3)-N(8)	2.167(10)	2.129(7)	
Fe(3)-N(12)	2.185(9)	2.194(6)	
Au(1)-C(1)	1.981(10)	1.997(8)	
Au(1)-C(3)	2.006(11)	1.991(8)	
Au(2)-C(2)	1.983(11)	1.985(8)	
Au(2)-C(5)	1.970(11)	1.977(8)	
Au(3)-C(6)	1.991(12)	2.000(8)	
Au(3)-C(7)	1.979(12)	1.980(9)	
Au(4)-C(4)	1.996(11)	1.981(8)	
Au(4)-C(8)	1.951(11)	1.990(8)	
Fe(1)-N(1)			2.154(6)
Fe(1)-N(2)			2.158(6)
Fe(1)-N(5)			2.201(6)
Fe(2)-N(3)			2.165(6)
Fe(2)-N(4)			2.162(6)
Fe(2)-N(6)			2.212(6)
Au(1)-C(1)			1.996(7)
Au(1)-C(3)			2.003(8)
Au(2)-C(2)			1.987(7)
Au(2)-C(4)			1.987(7)
N(1)-Fe(1)-N(2)	91.5(3)	92.0(3)	
N(1)-Fe(1)-N(9)	91.7(4)	91.3(3)	
N(2)-Fe(1)-N(9)	89.4(4)	89.2(3)	
N(3)-Fe(2)-N(4)	88.2(4)	88.0(2)	
N(3)-Fe(2)-N(5)	92.6(4)	94.0(2)	
N(3)-Fe(2)-N(6)	179.4(4)	179.4(2)	
N(3)-Fe(2)-N(10)	89.6(4)	89.9(2)	
N(3)-Fe(2)-N(11)	90.1(4)	89.7(2)	
N(4)-Fe(2)-N(5)	178.8(4)	177.6(2)	
N(4)-Fe(2)-N(6)	91.7(4)	92.2(2)	
N(4)-Fe(2)-N(10)	91.6(4)	91.9(2)	
N(4)-Fe(2)-N(11)	88.2(4)	87.6(2)	
N(5)-Fe(2)-N(6)	87.4(4)	85.8(2)	
N(5)-Fe(2)-N(10)	89.2(4)	89.4(2)	
N(5)-Fe(2)-N(11)	91.0(4)	91.1(2)	
N(6)-Fe(2)-N(10)	89.8(4)	89.5(2)	
N(6)-Fe(2)-N(11)	90.5(4)	90.8(2)	
N(10)-Fe(2)-N(11)	179.6(4)	179.4(2)	
N(7)-Fe(3)-N(8)	89.6(3)	89.8(3)	
N(7)-Fe(3)-N(12)	87.3(3)	87.6(2)	
N(8)-Fe(3)-N(12)	87.0(3)	87.9(2)	
C(1)-Au(1)-C(3)	175.1(4)	175.1(3)	
C(2)-Au(2)-C(5)	179.9(4)	179.4(3)	
C(6)-Au(3)-C(7)	173.9(5)	173.7(3)	
C(4)-Au(4)-C(8)	177.7(4)	176.7(3)	
N(1)-Fe(1)-N(2)			90.1(2)
N(1)-Fe(1)-N(5)			92.0(2)
N(2)-Fe(1)-N(5)			88.8(2)
N(3)-Fe(2)-N(4)			93.1(2)
N(3)-Fe(2)-N(6)			90.4(2)
N(4)-Fe(2)-N(6)			88.7(2)
C(1)-Au(1)-C(3)			175.8(3)
C(2)-Au(2)-C(4)			178.4(3)

Table S16. Crystal data for **AnPyAu·BrBz**.

	AuBrBz_90 K	**AuBrBz_165 K**	**AuBrBz_260 K**
Empirical formula	$C_{49.8}H_{32.5}Br_{1.3}N_6Au_2Fe$		
*M*r	1268.58		
Crystal system	orthorhombic		
Space group	*Pmna*	*Pmna*	*Ccc*2
a (Å)	14.6456(5)	14.7380(5)	14.6751(7)
b (Å)	14.3001(6)	14.3959(4)	22.7556(9)
c (Å)	22.5080(7)	22.5898(6)	14.9439(7)
V (Å^3)	4713.9(3)	4792.8(2)	4990.4(4)
Z	4		
D_c (mg cm^{-3})	1.787	1.758	1.688
F(000)	2411		
μ (Mo-K$_\alpha$) (mm^{-1})	7.654	7.528	7.230
Crystal size (mm)	0.10x0.30x0.30		
No. of total reflections	5643	5678	3880
No. of reflections [$I>2\sigma(I)$]	3485	3877	3236
R [$I>2\sigma(I)$]	0.1041	0.0848	0.0489
wR [$I>2\sigma(I)$]	0.2406	0.2117	0.1232
S	1.042	1.058	1.051

$R_1 = \Sigma \, ||Fo| - |Fc|| \, / \, \Sigma \, |Fo|$; $wR = [\, \Sigma \, [w(Fo^2 - Fc^2)^2] \, / \, \Sigma \, [w(Fo^2)^2]]^{1/2}$.
$w = 1/ \, [\sigma^2(Fo^2) + (m \, P)^2 + n \, P]$ where $P = (Fo^2 + 2Fc^2) \, / \, 3$;
m = 0.0740 (**1**), 0.0788 (**2**) and 0.0614 (**3**);
n = 260.7764 (**1**), 124.1095 (**2**) and 16.4940 (**3**)

Table S17. Selected bond lengths [Å] and angles [°] for **AnPyAu·BrBz**.

	AuBrBz_90 K	**AuBrBz_165 K**	**AuBrBz_260 K**
Fe-N(1)			2.14(2)
Fe-N(2)			2.11(2)
Fe-N(3)			2.247(5)
Fe(1)-N(1)	2.086(12)	2.155(9)	
Fe(1)-N(3)	2.15(12)	2.206(13)	
Fe(2)-N(2)	1.952(12)	1.944(9)	
Fe(2)-N(4)	2.01(2)	2.007(13)	
Au-C(1)	1.977(14)	1.992(11)	1.96(2)
Au-C(2)	2.031(14)	2.009(11)	2.15(2)
N(1)-Fe-N(2)			90.7(5)
N(1)-Fe-N(3)			89.3(5)
N(2)-Fe-N(3)			90.9(4)
N(1)-Fe(1)-N(3)	89.5(5)	88.9(3)	
N(2)-Fe(2)-N(4)	89.7(5)	89.7(4)	
C(1)-Au-C(2)	175.4(6)	175.2(5)	170.0(7)

Figure S8. Views along the *c* and the *a* directions of the orthorhombic **AnPyM·XBz** network

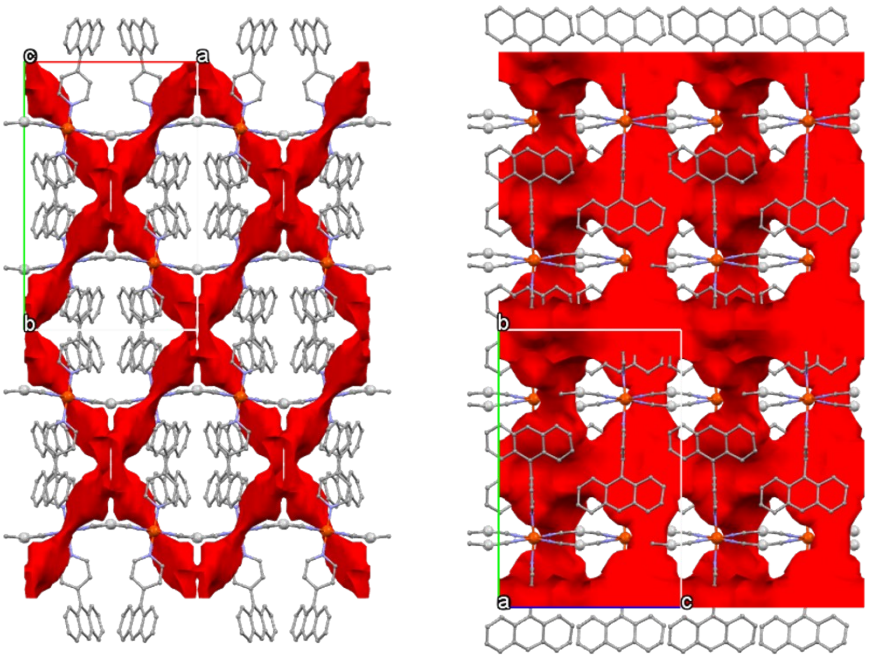

showing the solvent accessible surface.

Figure S9. Orthorhombic unit cell of **AnPyAg·CH_3Bz** at 120 K showing the arrangement of the toluene guest molecules in the two parallel channels, running along *c*-direction, generated by the interdigitation of the axial AnPy ligands of the 2D frameworks (excluded for simplicity)

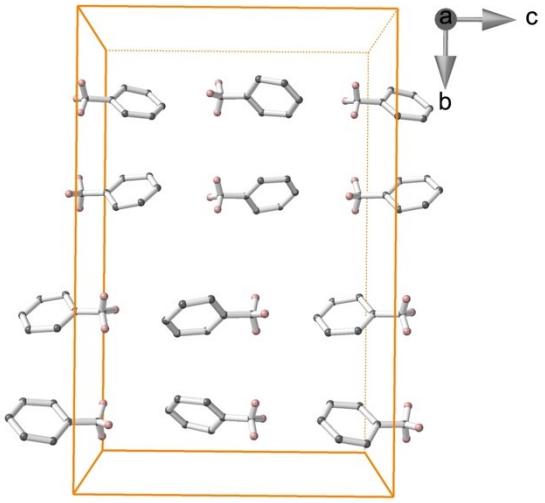

Figure S10. Structural ordering of the HS (red) and LS (blue) states responsible for the symmetry breaking observed in the plateau at 50% of spin state conversion for **AnPyAg·ClBz**, **AnPyAg·BrBz** and **AnPyAu·BrBz**.

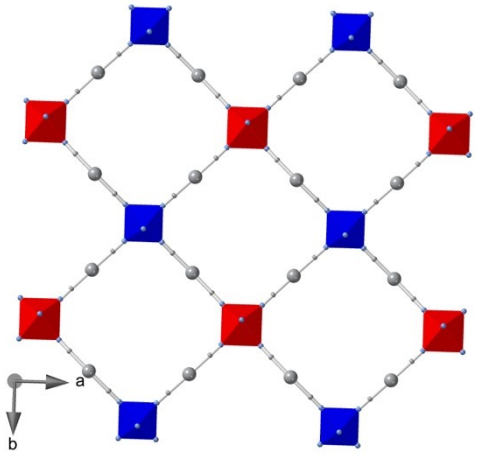

Figure S11. Fe^{II} environments observed for **AnPyM·XBz** in the a) *ccc2* (X=Cl (Ag),Br (Ag, Au)), b) *Pccn* (X=NO_2 (Ag, Au)) and c) *cmma* (CH_3 (Ag)) space groups and the corresponding d), e) and f) views

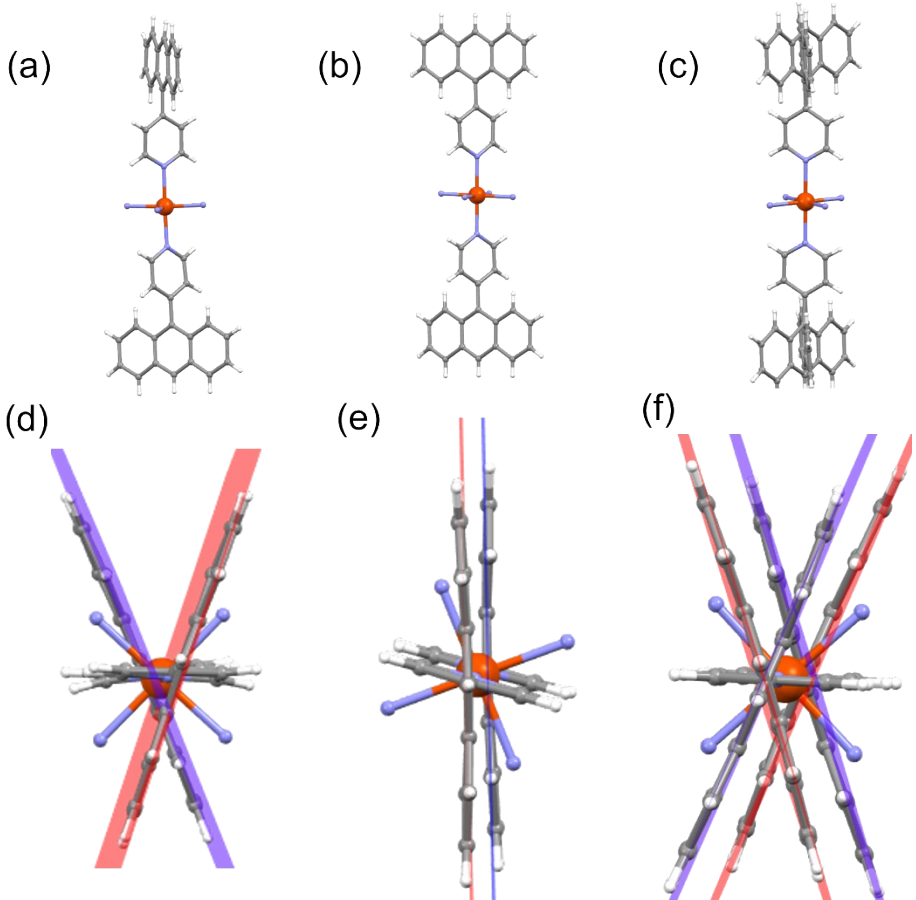

Figure S12. Packing of four consecutive layers of **AnPyAu·ClBz** view along *a*+*c* (left) / *b* (center, the guest molecules have been removed for clarity) and superposition of the layers on the *bc* plane (right).

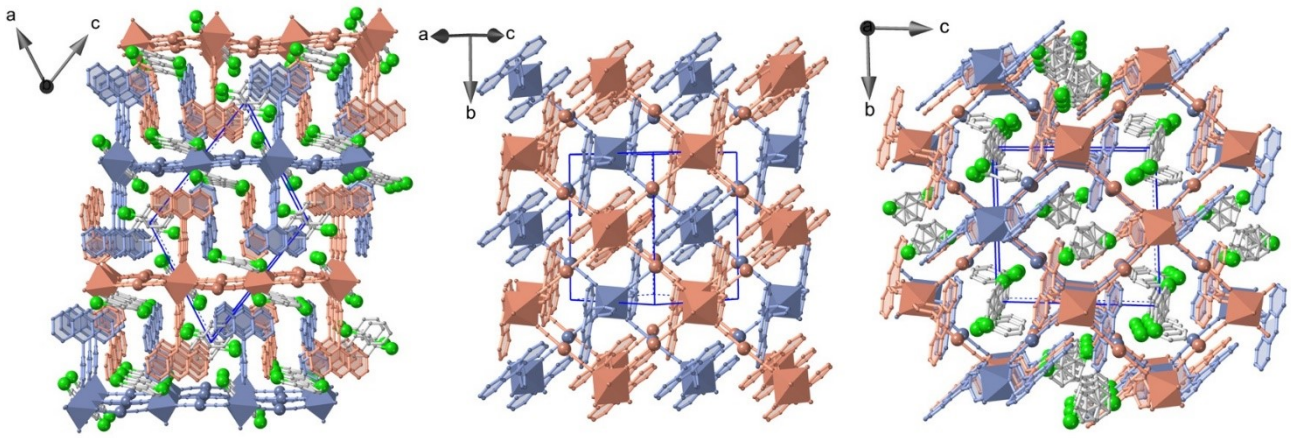

Figure S13. Distribution of the CH3Bz guests in channels 1 and 2 defined by the packing of the 2D polymeric frameworks in the triclinic form of **AnPyAu·CH_3Bz**.

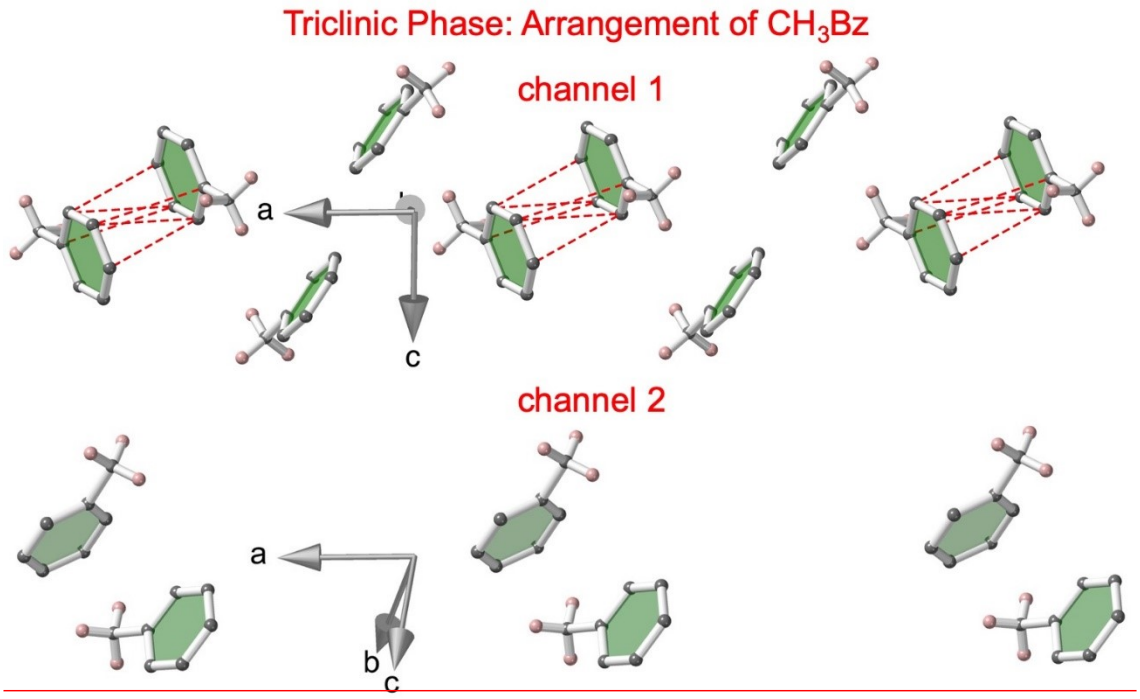

Table S18. Selection of short inter- and intra-layer distances for the triclinic forms of **AnpyAuCH$_3$Bz** and **AnpyAuClBz**

AnPyAu·CH$_3$Bz (triclinic)			
T / K	95 K	140 K	260 K
Anthracene···Anthracene (same layer)			
C36···C59	3.341	3.339	3.372
C36···C58	3.434	3.417	3.490
C37···C58	3.430	3.429	3.484
C37···C57	3.479	3.480	3.530
C38···C57	3.411	3.398	3.473
Anthracene···Anthracene (adjacent layers)			
C20···C53	3.357	3.392	3.439
C62···C61’	3.498	3.517	3.572
C24···C24’	3.426	3.452	3.537
Anthracene···Cyano (adjacent layers)			
C60···C6	3.356	3.363	3.433
C45···C5	3.384	3.430	3.472
AnpyAu·ClBz (triclinic)			
T / K	110 K	260 K	
Anthracene···Anthracene (same layer)			
C25···C38	3.414		
C21···C34’		3.491	
Anthracene···Anthracene (adjacent layers)			
C67···C37	3.313		
C67···C38	3.307		
C69···C17	3.431		
C70···C18	3.351		
C73···C16	3.319		
C75···C13	3.469		
C12···C12’		3.438	
C6···C34		3.499	
Anthracene···Cyano (adjacent layers)			
C18···C8	3.453		
C75···C2	3.480		

Figure S14. Thermal evolution of the *d-d* $^1A_1 \rightarrow {}^1T_1$ band in a single crystal during cooling 2 K/min of a) **AnPyAg·ClBz**, b) **AnPyAg·BrBz**, c) **AnPyAg·IBz**, d) **AnPyAg·NO_2Bz**, e) **AnPyAg·CH_3Bz**, f) **AnPyAu·ClBz**, g) **AnPyAu·BrBz**, h) **AnPyAu·IBz**, i) **AnPyAu·NO_2Bz** and j) **AnPyAu·CH_3Bz**. Notice that all of them exhibit an isosbestic point at around 650 nm indicating the change between the LS and HS compositions.

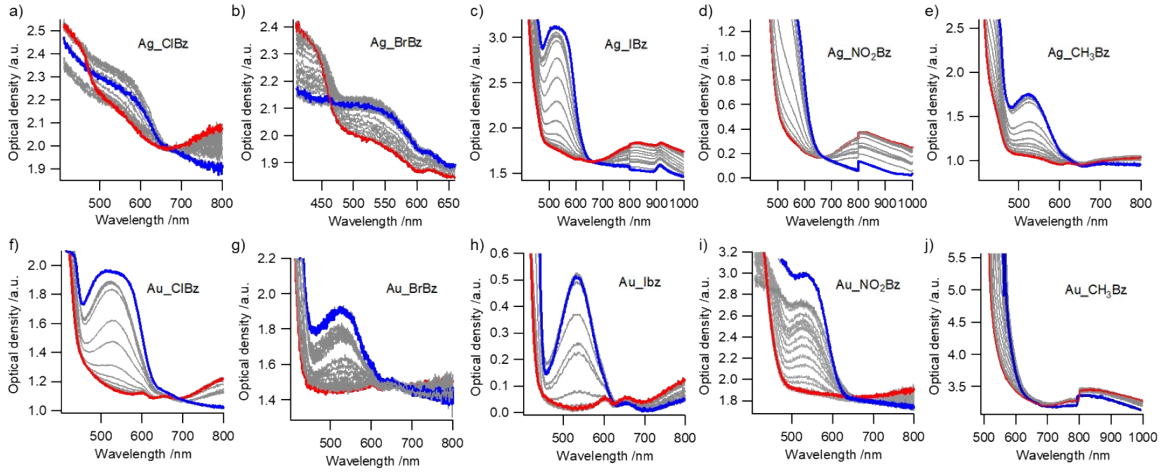

Table S19. Extinction coefficient of all the samples.

Sample	[] (M) (LS /HS)	Thickness (µm)	λmax LS (nm)	OD LS (lmax-717nm)	ε LS ($M^{-1}cm^{-1}$)	OD HS (717-799 nm)	ε HS ($M^{-1}cm^{-1}$)
Ag_ClBz	1.4302/1.3443	350	(SAT)	0.3604 (SAT)	7.1998	0.0779	1.6557
Ag_BzBz	1.4271/1.3351	350	(SAT)	0.1981 (SAT)	3.9660	0.0222	0.4751
Ag_IBz	----------	350	530	1.5186	----------	0.1225	----------
Ag_CH_3Bz	1.4247/1.3321	350	527	0.7768	15.578	0.0257	0.5512
Ag_NO_2Bz	1.4393/1.3344	350	(SAT)	1.306 (SAT)	25.925	0.1072	2.2953
Au_ClBz	1.3507/1.2673	350	522	0.8184	17.311	0.1118	2.5206
Au_BzBz	1.4091/1.3310	350	524	0.4943	10.023	0.0261	0.5603
Au_IBz	----------	350	531	0.5014	----------	0.0684	----------
Au_CH_3Bz	1.3126/1.2586	350	(SAT)	SAT PELLET	----------	0.0877	1.9908
Au_NO_2Bz	1.4246/1.3297	350	536	1.197	24.0064	0.0662	1.4225

Figure S15. Broadening of the hysteresis loop at increasing scan rates of temperature for **AnPyAu·BrBz**. The fact that the thermal spin transition temperature depends on the temperature scan rate indicates that the kinetics of the transition are slower than the temperature scan rate.

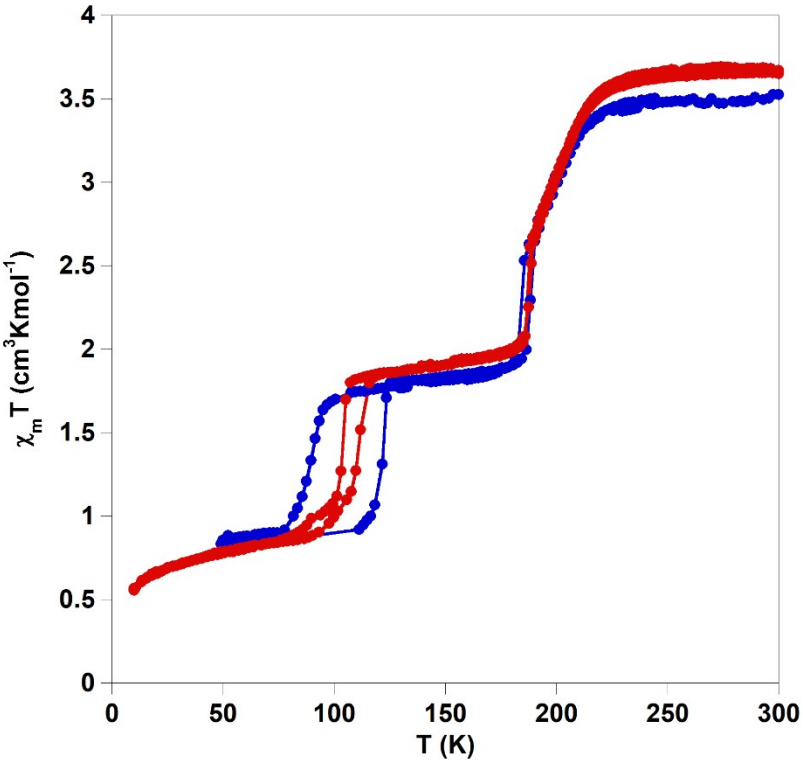

Figure S16. The thermal spin transition obtained optically for the semitransparent pellet of **AnPyAu·CH_3Bz** is more gradual due to the grinding and pressuring process. In fact, this effect has been undoubtedly attributed thanks to the comparison of the transition in **AnPyAg·IBz** as a crystal (a) and as diluted powder in a pellet (b). The corresponding thermal evolution of γ_{HS} is presented in (c).

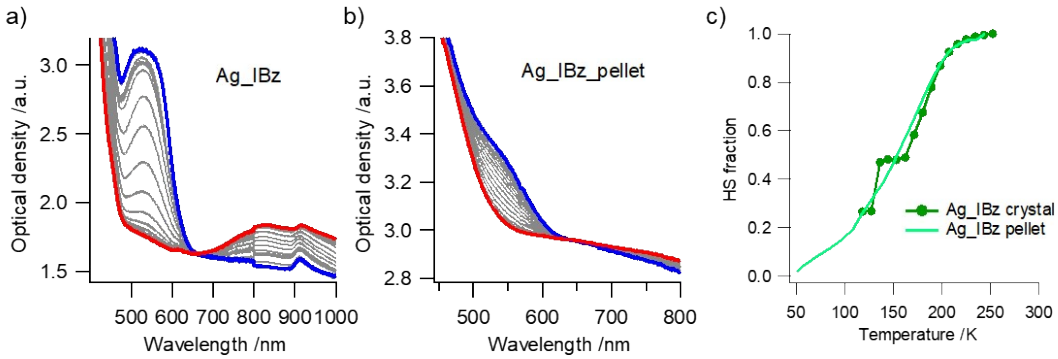

Figure S17. Comparison of the (a) room temperature excitation spectra (Inset: crystals measured dispersed in a copper plate), and b) room temperature and low temperature emission spectra at excitation 350 nm of an ensemble of **AnPyAg·IBz** crystals and of the previously studied fluorescent spin crossover compound {Fe(bpan)[Ag(CN)$_2$]$_2$} (Bpan = bis(4-pyridyl)anthracene) (see reference 60 in the main text). Both ligands exhibit the same features in the excitation and emission spectra but the excimer/exciplex signal is weaker in the case of AnPy ligand.

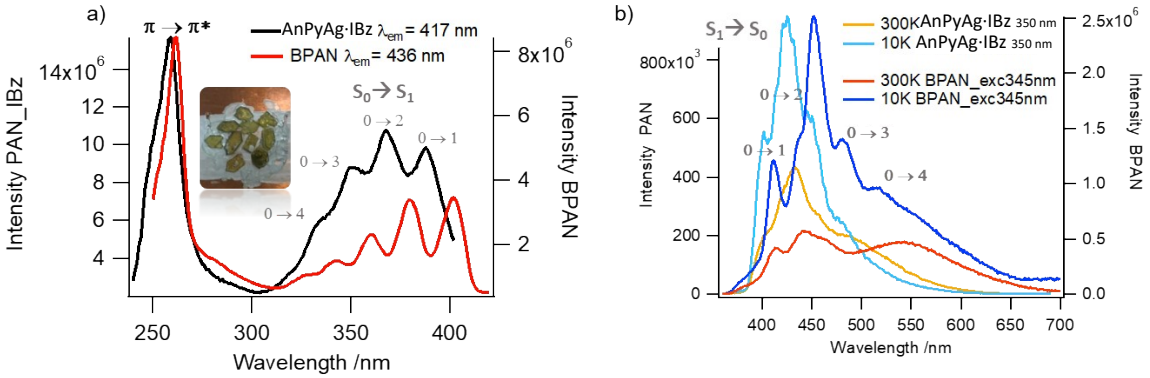

Figure S18. Emission spectra of the a) **AnPyAg·XBz** and b) **AnPyAu·XBz** crystals at excitation 365 nm at 300 K.

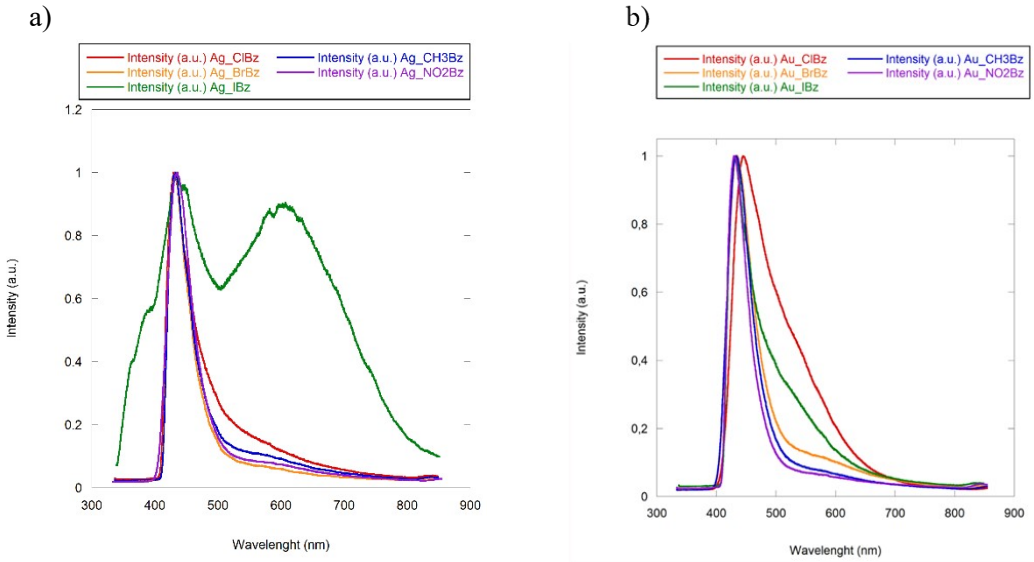

Figure S19. Spectra used for quantum yield estimation by an integrating sphere for AnPy.

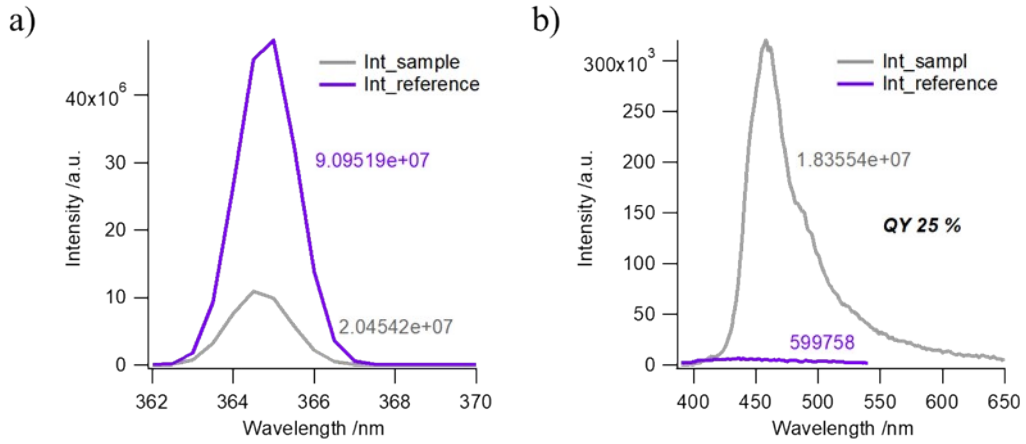

Figure S20. Thermal evolution of the emission spectra after excitation at 365 nm of an ensemble of crystals of a) **AnPy** and b) **NiAnPyAg·NO$_2$Bz** during cooling at 5 K/min with the corresponding variation of the intensity with the temperature for c) **AnPy** and d) **NiAnPyAg·NO$_2$Bz**.

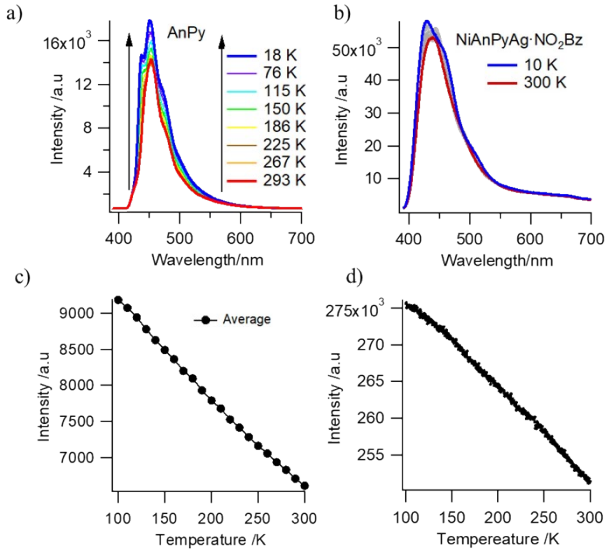

Figure S21. Thermal evolution of the emission spectra during heating at 5 K/min after excitation at 365 nm of an ensemble of crystals of a) **AnPyAg·CH_3Bz**, b) **AnPyAg·NO_2Bz**, c) **AnPyAg·BrBz**, d) **AnPyAg·ClBz,** e) **AnPyAu·CH_3Bz**, f) **AnPyAu·NO_2Bz** and g) **AnPyAu·BrBz**.

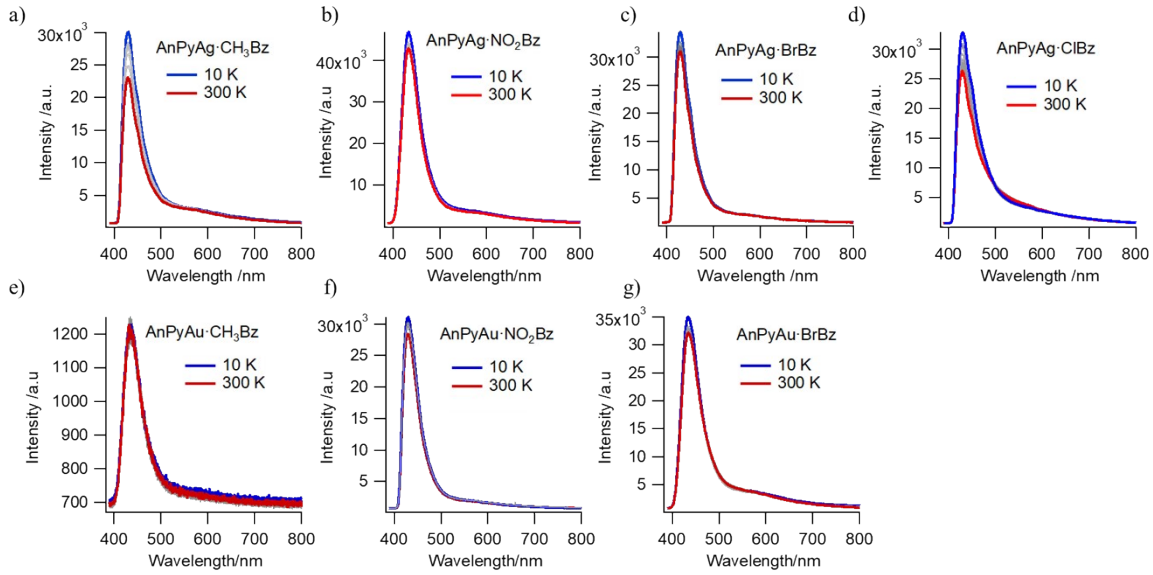

Figure S22. a) Thermal evolution of the emission spectra after excitation at 365 nm of an ensemble of crystals of **AnPyAu·ClBz** during heating at 5 K/min (Inset: Image of the emission of the crystals at room temperature) and b) the corresponding variation of the monomer and excimer/exciplex intensity with the temperature.

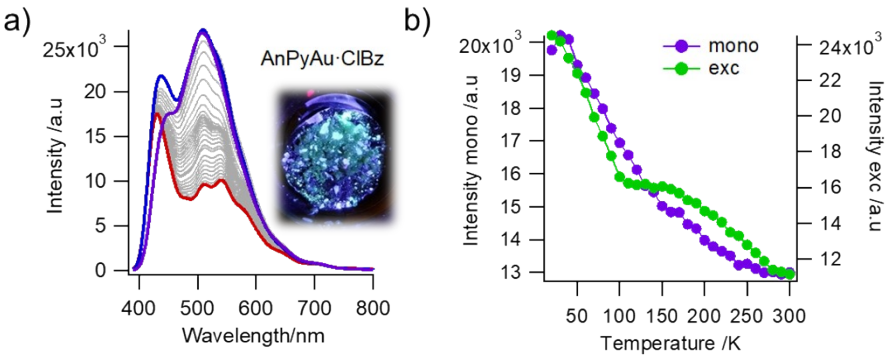

Table S20. Molecular volumes estimated through the Chimera software for the different studied guest

Guest	**V (Å^3)**
CH3Bz	87.9
NO2Bz	96.6
ClBz	96.4
BrBz	120.0
IBz	149.7